QUARTERLY JOURNAL OF THE ROYAL METEOROLOGICAL SOCIETY
Q. J. R. Meteorol. Soc. **134**: 199–215 (2008)
Published online 21 December 2007 in Wiley InterScience
(www.interscience.wiley.com) DOI: 10.1002/qj.182

Three-dimensional radiative transfer in midlatitude cirrus clouds

Wenyi Zhong,[a]* Robin J. Hogan[b] and Joanna D. Haigh[a]
[a] *Space and Atmospheric Physics, Blackett Laboratory, Imperial College London, UK*
[b] *Department of Meteorology, University of Reading, UK*

ABSTRACT: Three different types of cirrus cloud field, reconstructed in three dimensions directly from midlatitude observations by a cirrus stochastic model, are used to study the effects of three-dimensional radiative transfer in both the long-wave and short-wave spectral regions. Calculations of three-dimensional radiative transfer (3D), the independent column approximation (ICA) and the plane-parallel approximation are compared to quantify the effects on heating rates, radiative fluxes and related properties. Locally the heating rate difference between 3D and ICA reaches more than 10 K day^{-1} in both the long-wave and short-wave, depending upon the distributions of ice water content, which indicates that horizontal radiation transport plays an important role in structures of heating rate. The domain-averaged heating profiles of 3D agree within a few tenths of a K day^{-1} with ICA but show a systematic low bias. The domain-averaged heating rates in cloud layers are increased in 3D by up to 7% in the long-wave and more than 20% in the short-wave. The root-mean-square differences at individual points are up to ten times larger than the corresponding domain-averaged differences, representing the cancellation of opposing 3D effects. The ICA biases in long-wave net flux and emissivity have their maximum values (∼2–3%) near cloud top for the thinnest cloud with lowest fractional coverage. In general, ICA tends to reduce the reflected upwelling short-wave flux at the top of clouds; the layer-averaged albedo at cloud top agrees with 3D within 1%, although the corresponding RMS difference may differ by up to 30% from 3D at high solar zenith angles. Similar results are found for whole-sky (cloudy plus clear) short-wave reflectances and transmittances for which ICA agrees with 3D within 5%. For domain-averaged short-wave absorptance, however, ICA errors can reach 20%. The corresponding RMS differences may differ by up to 50% in reflectance and transmittance but exceed 200% in absorptance. The effects of solar zenith angle are also discussed. Copyright © 2007 Royal Meteorological Society

KEY WORDS independent column approximation; cloud heating rates

Received 22 March 2007; Revised 7 August 2007; Accepted 17 October 2007

1. Introduction

Cirrus clouds play an important role in weather and climate because of their global and persistent coverage. The effects of cirrus clouds on the Earth's radiation budget have been reviewed by Liou (1986) who concluded that cirrus clouds are one of the most important, yet least understood, atmospheric elements in weather and climate systems.

It is well known that the upper troposphere and lower stratosphere (UTLS) is a sensitive region where net heating rates are close to zero (Haigh, 1984). Small perturbations in heating may influence dynamical processes in the atmosphere, such as the organization of convection (Grabowski and Moncrieff, 2002; Tompkins and Di Giuseppe, 2003), cloud structure and evolution (Dobbie and Jonas, 2001) and mass transport (Corti *et al*., 2005). The distribution of net heating rate can also partially determine the distribution of many chemical constituents (e.g. ozone and water vapour) in the atmosphere (Dessler *et al*., 1996).

An important contribution to UTLS heating rate is made by cirrus cloud (Dessler *et al*., 1996) but, because of its inhomogeneous structure and its composition of non-spherical ice crystals, the calculation of radiative fields within cirrus is complex. The impact of assuming a plane-parallel geometry or of using the independent pixel approximation (or independent column approximation, ICA hereafter) in radiative transfer within broken cloud fields has been studied mainly for stratocumulus (e.g. Barker and Davies, 1992; Cahalan *et al*., 1994; Marshak *et al*., 1995). Full 3D radiative effects within realistic stratocumulus clouds have also been investigated (e.g. Hignett and Taylor, 1996; Di Giuseppe and Tompkins, 2003a) but 3D radiative transfer in cirrus cloud has received less attention. In those studies that do exist, the radiative effects of spatial structures have been calculated for two-dimensional cirrus clouds (Fu *et al*., 2000; Schlimme *et al*., 2005). Only Chýlek and Dobbie (1995) have studied the 3D radiative effects of cirrus on short-wave reflectivity and absorptivity. They used a Monte Carlo method but their idealized cirrus clouds

---

* Correspondence to: Wenyi Zhong, Blackett Laboratory, Imperial College, Prince Consort Road, London SW7 2AZ, UK.
E-mail: w.zhong@imperial.ac.uk

Copyright © 2007 Royal Meteorological Society

were not based on observations and were therefore not very realistic. Recent studies, however, have shown that the 3D cirrus structure significantly increases the global reflected solar fluxes at the top of atmosphere and therefore has an important impact on general-circulation model (GCM) simulations (Gu and Liou, 2006).

Recently new methods and computing models have been developed to quantify the influence of neighbouring clouds on the region considered and therefore to define the possible mechanisms (e.g. Várnai and Marshak, 2003; Nikolaeva *et al*., 2005). While these results have improved our understanding of 3D radiative transfer, their analyses are mostly in the short-wave region. So far 3D radiative effects of cirrus on long-wave radiative properties have not been well studied. Our simulations, discussed below, are not only in the short-wave but also in the long-wave region where cirrus clouds make large contributions to heating rates and other radiative fields.

Unlike in the short-wave region, long-wave radiation has a local source which is a function of the temperature structure. Thus upwelling thermal radiation from the surface and lower atmosphere play an important role in long-wave radiative transfer. In cirrus clouds, both emission and scattering of thermal radiation in three dimensions contribute to the changes of long-wave heating rate and other cloud radiative properties. Emission and scattering both depend on ice water content (IWC) and its distribution; the former is strongly related to temperature and the latter sensitive to size parameters and ice particle shape. As pointed out by Várnai and Marshak (2003), the 3D radiative transfer model we use does not provide the explicit photon paths, but our simulations can still quantify the 3D effects on long-wave heating rate and other properties such as long-wave emissivities and give indications of possible mechanisms whereby 3D radiative transfer influences those fields. Questions to be answered include: Does 3D radiative transfer tend to increase or decrease long-wave heating rate in the cloud, why and to what extent? Which column emissivities are enhanced or reduced? To what degree? How can 3D transfer affect these changes?

To study 3D radiative transfer in cirrus clouds, the impact of spatial structures is thus crucial. However, most observations of cirrus clouds are one- or two-dimensional. Because of limitations in sampling and observation it has been difficult to reproduce exactly observed 3D cirrus cloud structures. Cloud-resolving models also have problems in simulating realistic cirrus fall-streak structures (Marsham and Dobbie, 2005) as well as being computationally expensive.

Stochastic models are not only very useful to simulate 3D cloud structures for stratocumulus (DiGiuseppe and Tompkins, 2003b) and cumulus (Evans and Wiscombe, 2004), but have recently been successfully used to represent realistic cirrus cloud structures (Hogan and Kew, 2005). For example, DiGiuseppe and Tompkins (2003b) have applied 3D radiative transfer models to the clouds created by their stochastic stratocumulus model and found that the ICA biases depended upon the cloud coverage and horizontal spatial scales. For horizontal cloud scales below 5–10 km, the ICA bias became significant, and within a scale of 2 km, the ICA bias in flux-derived radiative fields could exceed 5%. For cirrus studies, 3D radiation has been used with contrails (Gounou and Hogan, 2007) but only ICA has been used with realistic 3D cirrus clouds. Here we present the first use of 3D radiative transfer with realistic cirrus structures. Based on the cirrus stochastic model of Hogan and Kew (2005), we perform 3D radiative transfer calculations to quantify cirrus cloud radiative effects.

In the second section of this paper we briefly describe how the cirrus cloud fields are reconstructed from observational data and the 3D radiative transfer code. In Sections 3 and 4 respectively, we discuss the long-wave and short-wave results for radiative heating rates, fluxes and related radiation fields. In Section 5 we draw our conclusions.

2. Model and data

The cirrus cloud fields used in this study were created by a 3D stochastic cloud model based on statistics derived from the radar observations from Chilbolton, southern England (Hogan and Kew, 2005). The stochastic model uses input profiles of the mean and fractional standard deviation of IWC, spectral slope, spectrum outer scale and wind speed as obtained from the observations. Isotropic 3D fractal fields are generated by an inverse 3D Fourier transform with random-phase coefficients, consistent with the observed 1D spectra. The model simulates horizontal displacement and changes to the spectra with height by manipulating and scaling the horizontal slices. The reconstructed 3D cirrus cloud fields are thus realistic in that they have the observed means and fractional standard deviations of IWC.

The stochastic model of Hogan and Kew (2005) is tightly constrained by the observations in that it reproduces not only the mean and the standard deviation, but also the precise shape of the power spectrum, which is the main thing required to produce realistic clouds. The random-phase assumption has a small effect on the ‘texture’ of the images. Figures 6–8 of Hogan and Kew (2005) demonstrate the ability of the stochastic model to reproduce the scale and amplitude of the cloud inhomogeneities that are important for radiative transfer.

The three 3D cirrus fields created are cases (1) 24 June 1999, (2) 27 August 1999 and (3) 27 December 1999. A summary of the properties of the three cirrus clouds can be found in Table I of Hogan and Kew (2005). The cloud heights are approximately from 6 to 9 km and domain-averaged visible optical depths are 1.2, 5.7 and 21.9 respectively. Figure 1 shows the ice water path (g m^{-2}) distributions for the three cases. Only case 1 has clear-sky columns in which the total ice water path from all layers is zero. The minimum column ice water paths are 2.48 g m^{-2} for case 2 and 160.59 g m^{-2} for case 3. The maxima of cloud fraction (IWC $> 10^{-3}$ g m^{-3}

Copyright © 2007 Royal Meteorological Society

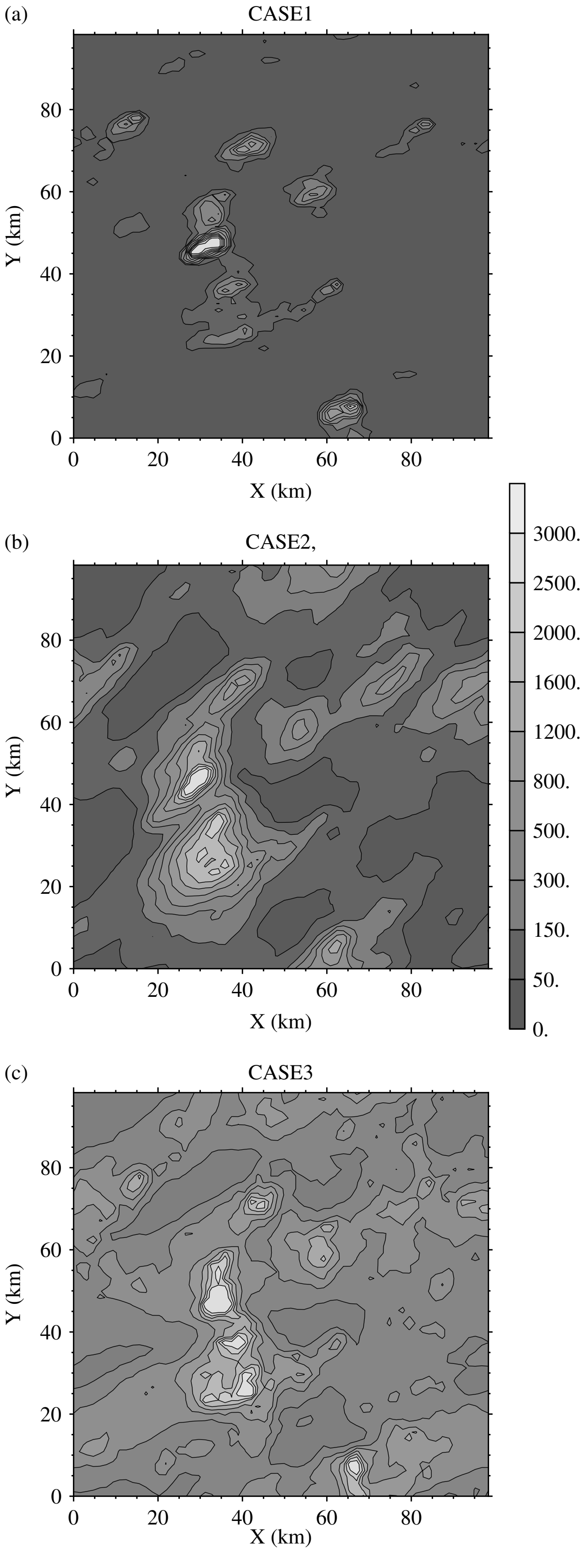

Figure 1. Ice water path (g m^{-2}) distributions for (a) case 1, (b) case 2 and (c) case 3.

at any height) are 0.51 (case 1), 1.00 (case 2) and 1.00 (case 3). Case 1 has the smallest generating level (Hogan and Kew, 2005) wind speed (15 m s^{-1}) and wind shear (3.5 m s^{-1} km^{-1}), case 3 the largest (56 m s^{-1} and 15.1 m s^{-1} km^{-1}) and case 2 intermediate (25 m s^{-1} and 5.0 m s^{-1} km^{-1}). These parameters introduce not only very different optical depths but also vertical structures including fall-streak geometry and shear-induced mixing.

The 3D radiative transfer model Spherical Harmonic Discrete Ordinate Method (SHDOM; Evans, 1998) is used for our study. SHDOM was chosen because we are interested in the spatial structure of the change to the radiation (as well as domain-averaged radiation fields), for which SHDOM is more accurate than Monte Carlo methods. Previous studies showed that the cloud geometry may have important effects on the ICA bias in particular when the scale of organization becomes less than 10 km (e.g. Di Giuseppe and Tompkins, 2003b). Another reason is that we prefer to use the same 3D model for both the long-wave and short-wave calculations but most Monte Carlo models do not include the long-wave region which is of crucial importance for cirrus clouds.

The angular resolution used for our calculations is 8 zenith and 16 azimuth integration angles. We assume a constant effective radius of 50 μm throughout the cloud. The scattering phase function was calculated with the ice parametrization of Yang *et al.* (2000) for the short-wave and Mie theory for the long-wave components. We use solid columns as the ice crystal shape for all short-wave calculations, but also tested the sensitivity to the use of bullet-rosettes.

The broadband calculations use the correlated k-distribution Rapid Radiative Transfer Model (RRTM; Mlawer *et al.*, 1997). There are 16 bands for the long-wave region (1000 to 3.33 μm) and 14 for the short-wave (0.2 to 12.195 μm). The Standard Atmosphere profile (McClatchey *et al.*, 1972) is used and the gaseous absorption is horizontally homogeneous. The surface short-wave albedo is set to 0.15 and the surface long-wave emissivity to 0.98. Solar zenith angles (SZAs) of 0, 20, 40, 60, 80° are calculated.

The horizontal resolution used in this study is about 1.56 km over a square domain of 100×100 km. The vertical resolution used is 60 m within and 1 km outside the clouds, but with 120 m used near cloud boundaries (between approximately 6 and 6.5 km, and 8.5 and 9.5 km). The total number of layers is around 60 from the surface to 30 km height. Periodic conditions are used for the horizontal boundaries. The simulated cirrus fields are also periodic.

To quantify the effects of horizontal photon transport and cloud inhomogeneity, we also perform ICA and plane-parallel (hereafter '1D') calculations. ICA calculations have same parameter settings as 3D except they assume local periodic boundary conditions in each of 64×64 columns. Thus the calculations are the same as in the 3D method but there are no horizontal exchanges of radiative energy between the columns. Therefore it does not matter whereabouts each independent column is located within the cloud domain. Unlike Hogan and Kew (2005), our plane-parallel 1D calculations simply use the layer-averaged IWC and do not divide each layer into cloudy and clear fractions, therefore no cloud overlap method is considered.

Copyright © 2007 Royal Meteorological Society

3. Long-wave results

3.1. Heating rate

In general, all three cases produce long-wave cooling in the upper regions of the clouds, due to emission, and heating in the lower regions, resulting from the trapping of upward infrared fluxes emitted by the surface and atmosphere. The distributions of heating rate differ markedly from case to case depending upon the spatial structure of IWC.

Figure 2(a, d, g) show the layer-averaged heating rate profiles from 3D and ICA calculations, together with the 1D results obtained from the layer-averaged IWC profiles. There are large differences between 1D and ICA heating rates, similar to the results of Hogan and Kew (2005) for ICA and 1D. The differences between 3D and ICA are small and are therefore presented in Figure 2(b, e, h). The ICA agrees with 3D to within 0.1 K day^{-1} for cases 1 and 2, and within 0.5 K day^{-1} for case 3 but a cooling bias dominates the ICA results.

Table I presents the averaged cloud heating rates in the upper (8–9.5 km) and the lower (6–7 km) cloud layers. These are the differences between the total

Table I. Mean long-wave cloud heating rate (K day^{-1}) and the ICA bias in two height ranges for three cirrus cases.

	8–9.5 km		6–7 km	
	3D	ICA−3D	3D	ICA−3D
Case 1	−0.52	−0.01 (2%)	0.98	−0.07 (7%)
Case 2	−3.15	−0.02 (1%)	4.00	−0.04 (1%)
Case 3	−7.63	−0.30 (4%)	9.93	0.00 (0%)

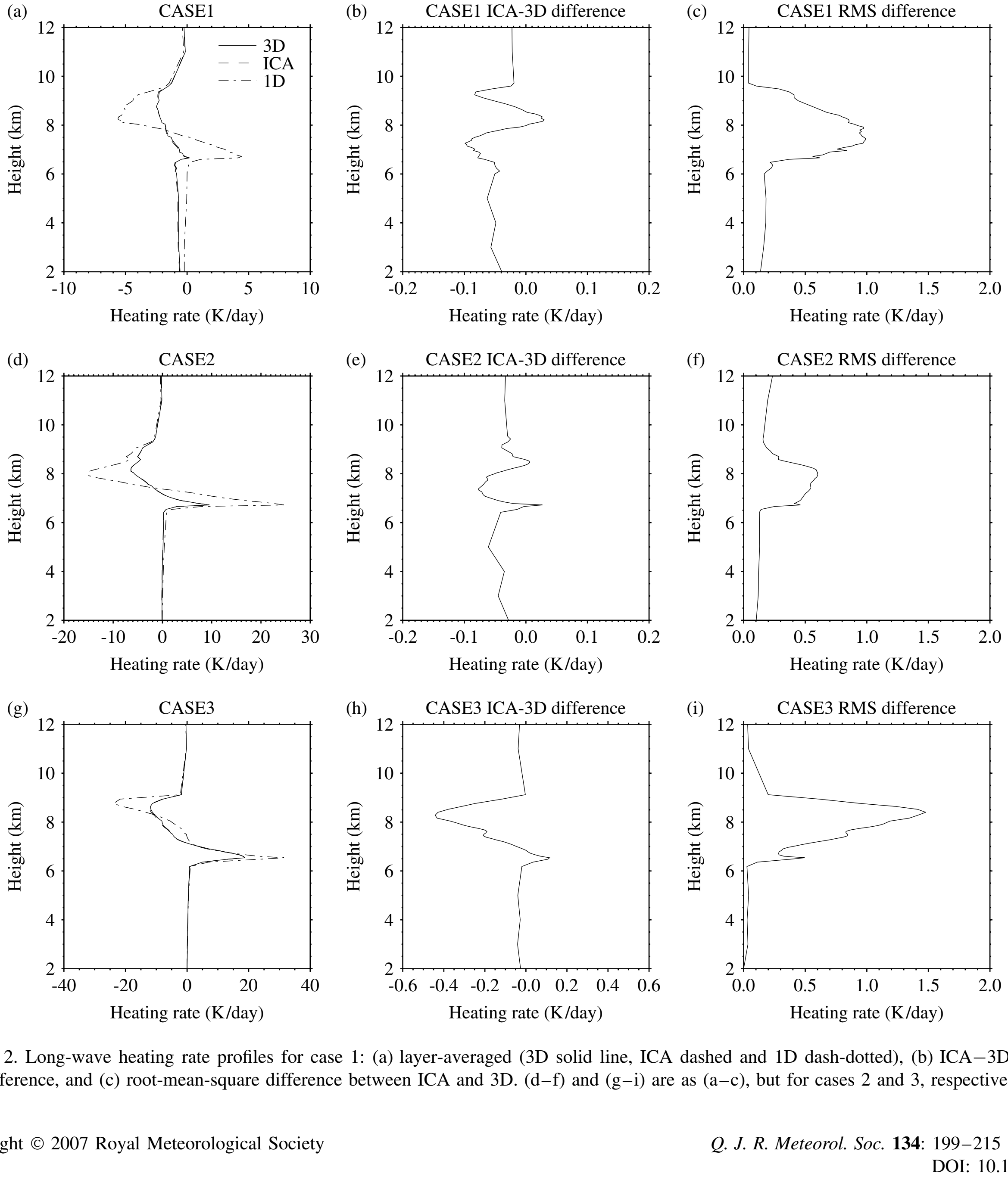

Figure 2. Long-wave heating rate profiles for case 1: (a) layer-averaged (3D solid line, ICA dashed and 1D dash-dotted), (b) ICA−3D mean difference, and (c) root-mean-square difference between ICA and 3D. (d–f) and (g–i) are as (a–c), but for cases 2 and 3, respectively.

Copyright © 2007 Royal Meteorological Society

(cloud+clear−sky) and clear-sky heating rates. On average, ICA overestimates long-wave cooling with the largest absolute difference (0.3 K day^{-1}) in the upper layer of case 3, but the largest percentage difference (7%) in the lower layer of case 1.

The results in Figure 2 and Table I show that the introduction of 3D transport tends to increase the heating rate in the cloud. This can be explained by the fact that in 3D, upwelling thermal radiation from lower in the atmosphere has a greater chance to enter the cloud and be absorbed than in ICA because it can enter a cloud through the sides. This mechanism was used by Gounou and Hogan (2007) to explain why aircraft contrails have a larger radiative forcing in the long-wave region when 3D transport is included. In the more complex cloud scenes considered here, there is often not so much of a division between cloudy and clear air, but rather between optically thick and optically thin regions. In such a configuration the same mechanism can act, but a counter mechanism can also play a role whereby cloud elements that are shielded from upwelling radiation are more able to cool by emission from cloud sides, leading to some parts of the profile in Figure 2 where the introduction of 3D transport tends to reduce the heating rate.

Figure 2(c, f, i) present the within-layer root-mean-square (RMS) difference between 3D and ICA for the three cases. Case 3 shows the largest difference with a maximum of 1.5 K day^{-1}, case 2 the smallest with a maximum of 0.6 K day^{-1} with case 1 having a maximum of 1 K day^{-1}. They are much larger than the layer-averaged differences in Figure 2(b, e, h), indicating that there is significant cancellation between large anomalies of opposite sign.

We now plot 2D slices of case 3 (27 December 1999) to illustrate the structure of long-wave heating rate. Figure 3(a) is the heating rate $x-z$ cross-section arbitrarily chosen at $y = 36$ km and Figure 3(b) the heating rate averaged over the y direction. It can be seen that, for individual grid points, the maximum cooling reaches nearly −50 K day^{-1} and maximum heating about 40 K day^{-1}. The other two cases (not shown) have similar maxima because heating rates are mainly determined by the IWC in cloud cells which have similar range of IWC in each case. IWC is indicated by the shading in Figures 3(a) and (b). We present y-direction averaged heating rates in order to see the effects of the averaging on the magnitude of the heating rate and the ICA bias. It is difficult to quantify 3D effects from 2D cloud fields, but most existing results concerning the radiative effects of cirrus inhomogeneity are obtained from 2D studies. It can be seen that the y-direction averaged heating rates have a much smaller range than those of Figure 3(a) (within ±3 K day^{-1} for case 1 and ±20 K day^{-1} for cases 2 and 3). While the ranges of heating rate are similar among the three cases, the maxima and minima of y-averaged heating rates are significantly different from case to case and related to the optical thickness in the clouds.

Figures 3(c) and (d) show the heating rate differences between ICA and 3D for the situations in Figures 3(a) and (b) respectively. In Figure 3(c) the differences in heating rate are within a few K day^{-1}. This is also true for case 2 but they exceed 20 K day^{-1} for case 1 (not shown), which has the smallest optical depth. This indicates that ICA−3D differences do not depend primarily upon the total optical thicknesses but on local IWC and that a relatively small cloud cover may have

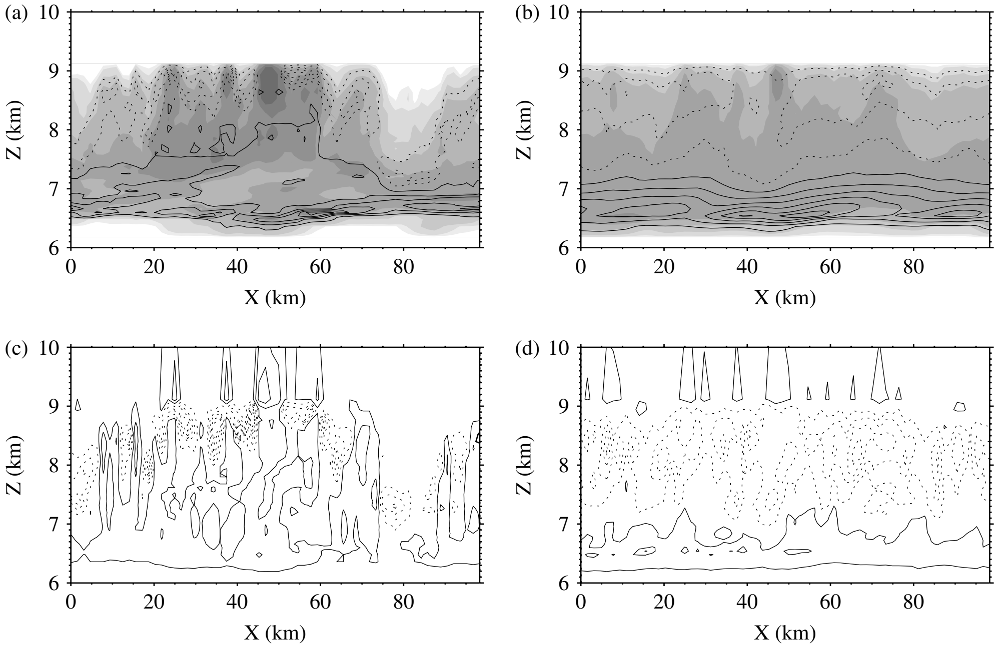

Figure 3. (a) $x-z$ cross-section of long-wave heating rate at $y = 36$ km for case 3: contour interval is 10 K day^{-1} and negative contours are dashed. Shading indicates ice water content (light to dark) at 0.001, 0.003, 0.01, 0.03, 0.1, 0.3 g m^{-3}; (b) is as (a) but averaged along the y direction; the contour interval for heating rate is 5 K day^{-1}; (c) is as (a) but for the difference ICA−3D, with contour interval 1 K day^{-1}; (d) is as (b) but for the difference ICA−3D, with contour interval 0.2 K day^{-1}.

Copyright © 2007 Royal Meteorological Society

DOI: 10.1002/qj

a larger absolute 3D effect within the clouds. For the y-averaged sections, ICA−3D differences in heating rate (Figure 3(d)) are much smaller; case 3 has the largest value (~ -1 K day^{-1}) while the other two cases are within 0.5 K day^{-1}.

Figure 4 shows scatterplots of ICA versus 3D heating rates for all the pixels in the top cloud layer (~9 km) and base layer (~6.5 km) for the three cases. The spread exceeds 5 K day^{-1} and, in general, the ICA−3D differences near cloud-top layers are larger than those in the layers near cloud base. For the cases studied here, 3D radiative effects are more significant near cloud top for long-wave heating rates.

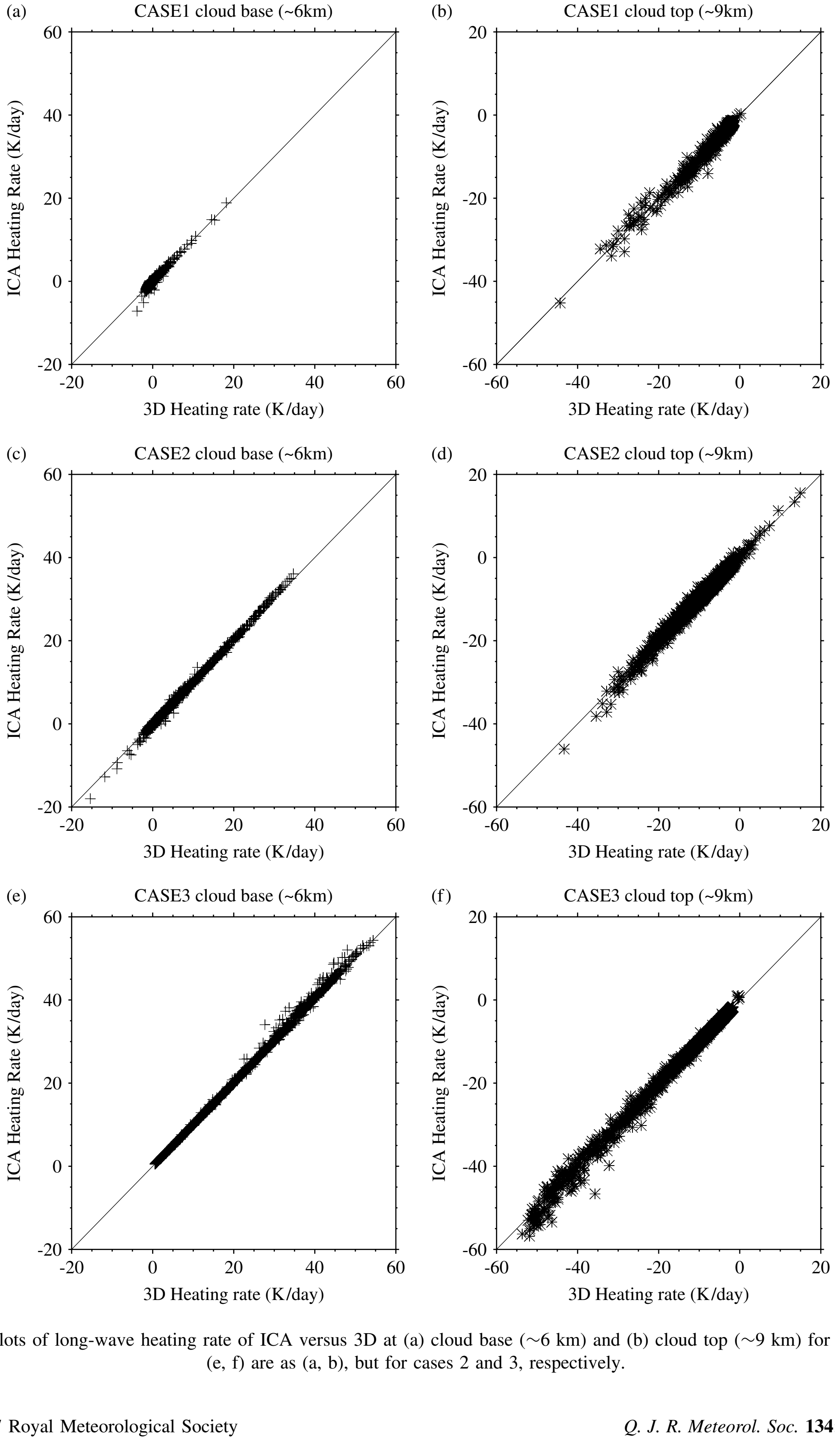

Figure 4. Scatterplots of long-wave heating rate of ICA versus 3D at (a) cloud base (~6 km) and (b) cloud top (~9 km) for case 1. (c, d) and (e, f) are as (a, b), but for cases 2 and 3, respectively.

Copyright © 2007 Royal Meteorological Society

DOI: 10.1002/qj

3.2. Long-wave fluxes and emissivity

Table II presents the layer-averaged values. As might be expected from the optical depths, case 1 has the largest outgoing long-wave flux and ICA bias and case 3 the smallest. Figure 5 presents the ICA−3D differences in net long-wave fluxes at the top of cloud; again case 1 also shows the greatest, and case 3 the least, variability. This indicates that the horizontal flux transport, and thus largest potential for errors in using ICA, is determined by cloud structure rather than by the magnitude of the optical depth.

Table II. 3D mean long-wave net flux (W m^{-2}) just above cloud top.

	3D mean net flux	ICA−3D	$\frac{\text{ICA}-\text{3D}}{\text{3D}}$	RMS difference
Case 1	199.88	2.13	1.1%	6.65
Case 2	166.82	0.99	0.6%	3.16
Case 3	135.66	0.48	0.4%	1.75

Cirrus clouds cannot be treated as black bodies in the long-wave region and scattering processes must be

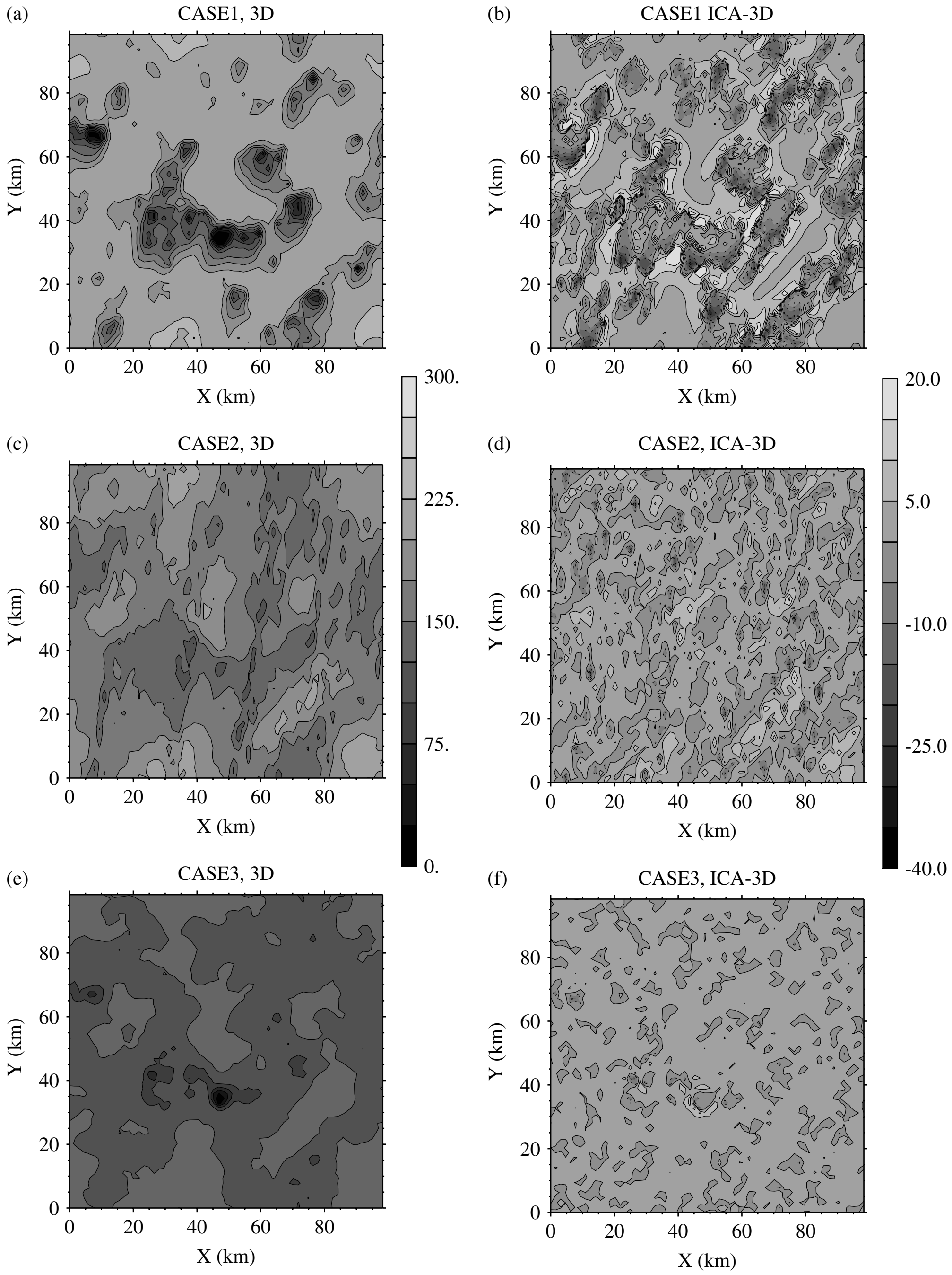

Figure 5. (a) 3D long-wave net fluxes, with contour interval 30 W m^{-2}, and (b) ICA−3D differences in long-wave net fluxes, with contour interval 3 W m^{-2}, both at cloud top in case 1. (c, d) and (e, f) are as (a, b), but for cases 2 and 3, respectively.

Copyright © 2007 Royal Meteorological Society

taken into account because they are composed of large ice crystals (and therefore have a larger ratio of size to wavelength) with low number densities (longer photon free path). We use the following equations to calculate the emissivity (Liou, 1986):

$$\epsilon^{\uparrow}(z_t) = [F^{\uparrow}(z_t) - F^{\uparrow}(z_b)]/[\sigma T_t^4 - F^{\uparrow}(z_b)], \quad (1)$$

$$\epsilon^{\downarrow}(z_b) = [F^{\downarrow}(z_b) - F^{\downarrow}(z_t)]/[\sigma T_b^4 - F^{\downarrow}(z_t)], \quad (2)$$

where $\epsilon^{\uparrow}(z_t)$ and $\epsilon^{\downarrow}(z_b)$ are the upward emissivity at cloud top and the downward emissivity at the base of cirrus respectively. $F^{\uparrow}$ and $F^{\downarrow}$ are the upwelling and downwelling long-wave fluxes; T_t and T_b are the cloud-top and cloud-base temperatures; z_t and z_b are cloud-top and cloud-base heights respectively and σ is the Stefan–Boltzmann constant.

For layer averages it is found that there is negligible difference between the results of taking an average of 2D emissivities (calculated from 3D results for each column then averaged over all columns) and calculating the emissivity from area-averaged fluxes. The latter method is used here.

Figure 6 shows scatterplots of 3D versus ICA calculations for upward emissivities at cloud top for the three cases. For case 1 the emissivity ranges from 0.1 to 1.0 with a maximum spread of 0.3, for case 2 from 0.05 to 0.9 with spread 0.2, and for case 3 from 0.6 to 0.9 with spread 0.1.

Figure 6 also shows scatterplots for downward emissivities at cloud base for the three cases. Case 3 has the largest minimum (∼0.91) and case 1 and 2 have minima ∼0.3. The three cases have similar maxima (>0.95). Case 1 has the largest spread (>0.2) and case 3 the smallest spread (<0.05).

It can be seen in Figure 6 that ICA tends to overestimate emissivity for the upper parts (where emissivities are larger) and underestimate it for the lower parts (where emissivities are lower). The higher emissivities represent the thicker clouds and the lower ones the thinner clouds or clear sky; ICA emits more in the former case and less in the latter because ICA has no horizontal transport of radiation between columns. In other words, the emissivities of thinner columns are enhanced due to the introduction of 3D radiative transfer, because more thermal radiation can go into than out from them, whereas for thicker areas emissivities tend to be reduced by 3D effects.

Comparing Figures 4 and 6, we also see that the emissivities are more scattered than long-wave heating rates. Because emissivities are calculated based on the whole column but heating rates are evaluated for each grid point, the deviation of ICA from 3D for emissivity is greater than that for heating rate.

The layer-averaged upward and downward emissivities, and comparison with the 1D results, are given in Tables III and IV respectively. The ICA method gives better than 1% accuracy for both $\epsilon^{\uparrow}(z_t)$ and $\epsilon^{\downarrow}(z_b)$ for both cases 2 and 3. However, for case 1, errors are 1.6% (downward) and 3.4% (upward). For case 3, in which the cloud base is optically thick and so behaves almost as a black body, the 1D method is satisfactory. For cases 1 and 2, and for the upward emissivity at the cloud top in case 3, the 1D method gives large errors.

4. Short-wave results

4.1. Heating rates

We now discuss the short-wave results. Figure 7(a, d, g) show the heating rate profiles from the layer-averaged 3D and ICA, and for SZA=0° and 60°. 1D results, obtained from the layer-averaged IWC profiles, are also plotted for comparison. As expected, the heating rates for SZA=60° are much smaller than those for SZA=0° for all cases because the incoming short-wave flux is halved. As for the long-wave heating rates, the differences between 3D and ICA are small, so in Figure 7(b, e, h) the differences ICA−3D for the two SZAs are presented. The ICA agrees with 3D to within 0.1 K day^{-1} for all experiments except case 3 with SZA=60°, where the difference exceeds 0.2 K day^{-1}.

Figure 7(c, f, i) present the RMS differences between ICA and 3D for the three cases. It shows that the RMS differences of SZA=60° are much larger than those of SZA=0° for all cases. The figure, plus calculations for other solar zenith angles (not shown), demonstrate that between SZA=0° and 60° the larger the SZA, the more significant the 3D effects. For SZA=80° the RMS differences change little (for case 1) and decrease (cases 2 and 3) by up to 20% from those at SZA=60°, but relative to heating rate their differences are still the largest. For the absolute RMS difference, case 3 has the largest value with maximum of 1.9 K day^{-1} for SZA=60° and 0.9 K day^{-1} for SZA=0°, case 2 the smallest with maximum 1 K day^{-1} (SZA=60°) and 0.5 K day^{-1} (SZA=0°), and case 1 intermediate with maximum 1 K day^{-1} (SZA=60°) and 0.7 K day^{-1} (SZA=0°). For the percentage change, case 1 is the largest and case 2 the smallest for both heating rate difference and the RMS difference.

Table III. Upward emissivity at cloud top.

	Emissivity	ICA−3D	$\frac{\text{ICA}-\text{3D}}{\text{3D}}$	1D	$\frac{\text{1D}-\text{3D}}{\text{3D}}$
Case 1	0.3430	−0.0118	3.4%	0.7040	105%
Case 2	0.5376	−0.0015	0.3%	0.8668	61%
Case 3	0.7539	−0.0006	0.1%	0.9533	26%

Table IV. Downward emissivity at cloud base.

	Emissivity	ICA−3D	$\frac{\text{ICA}-\text{3D}}{\text{3D}}$	1D	$\frac{\text{1D}-\text{3D}}{\text{3D}}$
Case 1	0.4725	−0.0079	1.6%	0.7466	58%
Case 2	0.7233	−0.0017	0.2%	0.9551	32%
Case 3	0.9753	−0.0001	<0.1%	0.9796	0.4%

Copyright © 2007 Royal Meteorological Society

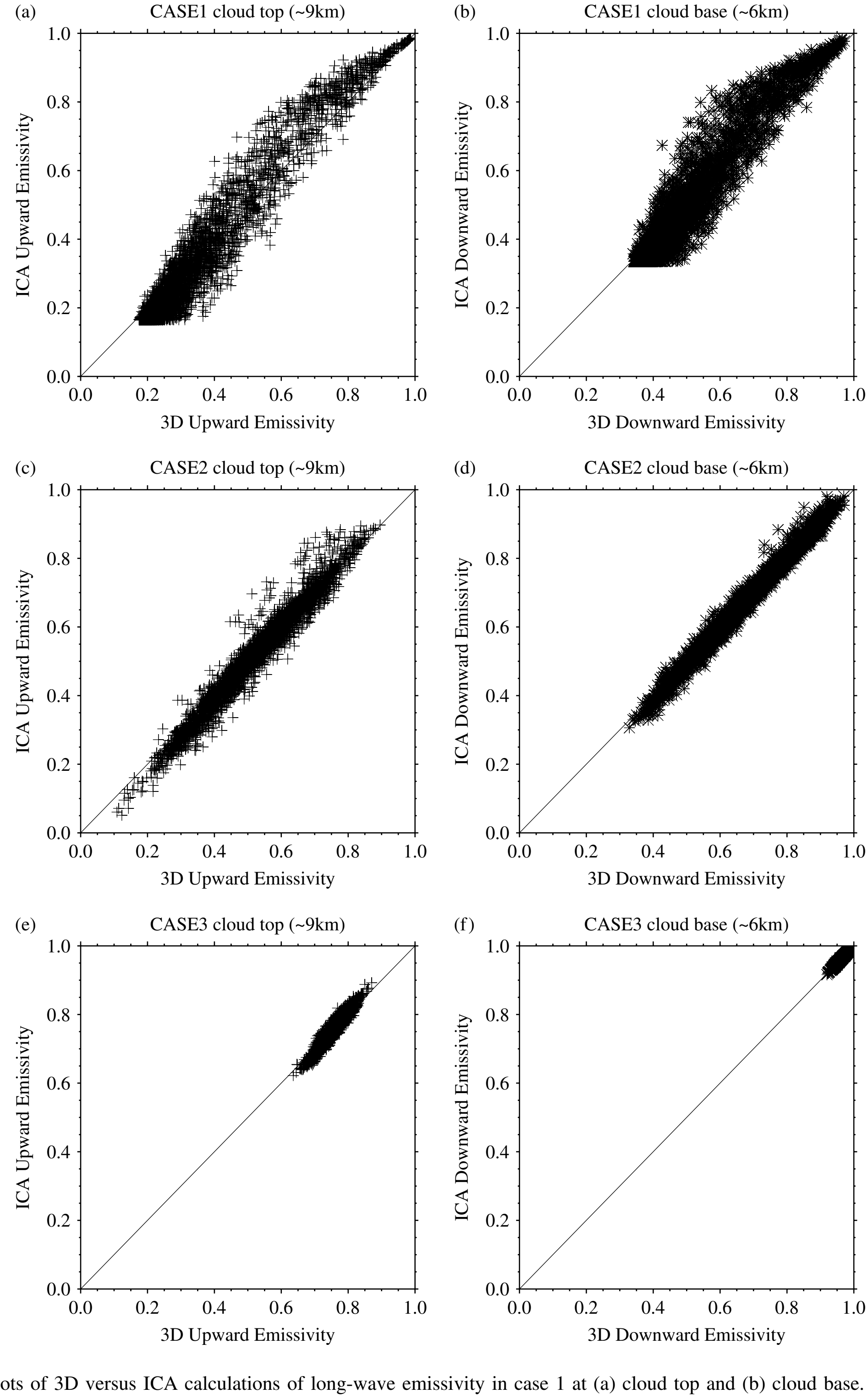

Figure 6. Scatterplots of 3D versus ICA calculations of long-wave emissivity in case 1 at (a) cloud top and (b) cloud base. (c, d) and (e, f) are as (a, b), but for cases 2 and 3, respectively.

Table V presents domain-averaged (over all x and y points and $z = 6$–9.5 km) heating rates and the RMS difference between ICA and 3D calculations. These represent the heating rates of cloud only, i.e. the differences between the total (cloud+clear−sky) and clear-sky heating rates. The domain-averaged heating rate is equivalent to the total short-wave radiation absorbed by the cloud in the domain. In the majority of results in cases 1 and 2, the ICA heating rates are less than the corresponding 3D result (up to 23% and 6% in cases 1 and 2, respectively), indicating that horizontal fluxes existing in 3D modelling contribute significantly more heating. However, in case 3 (the thickest cloud among the three), ICA domain-averaged heating rates are larger than those of 3D except for SZA=0°, indicating the sign of ICA−3D in domain-averaged heating rate may be related to the cloud optical thickness and the albedo of the cloud top, and also to the SZA. The RMS differences are much larger than

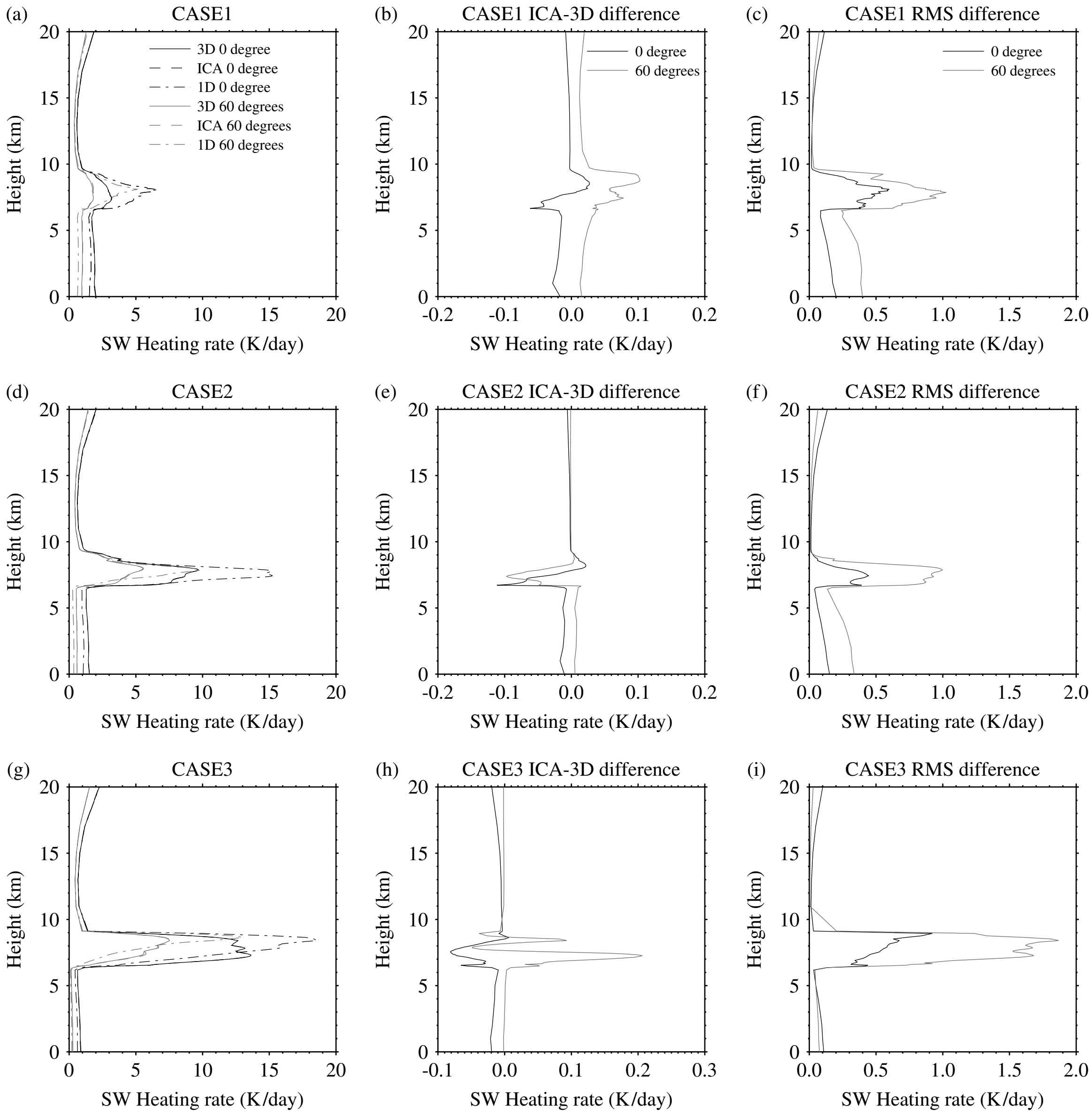

Figure 7. As Figure 2 but for short-wave heating rates at two solar zenith angles: 0° (black) and 60° (grey).

Table V. Domain-averaged 3D heating rate (K day^{-1}), difference between ICA and 3D and their RMS difference.

SZA	Case 1			Case 2			Case 3		
	3D	ICA−3D	RMS	3D	ICA−3D	RMS	3D	ICA−3D	RMS
0°	1.03	−0.01 (−1%)	0.40 (39%)	4.75	−0.02 (−0%)	0.28 (6%)	8.53	−0.05 (−1%)	0.50 (6%)
20°	0.97	0.00 (0%)	0.54 (56%)	4.52	−0.21 (−5%)	0.68 (15%)	7.89	0.04 (1%)	0.88 (11%)
40°	0.83	−0.01 (−1%)	0.67 (84%)	3.83	−0.02 (−1%)	0.56 (15%)	6.19	0.06 (1%)	1.26 (20%)
60°	0.51	0.06 (12%)	0.74 (145%)	2.59	−0.03 (−1%)	0.73 (28%)	3.50	0.06 (2%)	1.37 (39%)
80°	0.22	−0.05 (−23%)	0.68 (309%)	0.68	−0.04 (−6%)	0.59 (88%)	0.51	0.03 (6%)	0.81 (159%)

ICA−3D and the RMS percentage difference increases significantly with SZA for all three cases.

Figure 8(a) shows the $x - z$ cross-section of short-wave heating rate for $y = 36$ km, SZA=60°, chosen as illustrative of the structure. For individual grid points, the maximum heating reaches ∼30 K day^{-1} for all three cases but the heating rate structure varies from case to case and with SZA. Case 1 has a much smaller region than the other two cases (not shown), where heating exceeds 25 K day^{-1}. For larger SZA, the heating is much weaker than when the sun is overhead. Unlike in the long-wave, the short-wave heating rates in clear sky below the

Copyright © 2007 Royal Meteorological Society

cirrus clouds are significantly influenced by the cloud structures, in particular in illuminated and shadowed regions.

For y-averaged $x - z$ sections, heating rates are much smaller with maxima about 5 K day^{-1} for SZA=0° and 3 K day^{-1} for SZA=60° in case 1; 10 K day^{-1} for a significant proportion of the domain (SZA=0°) and 8 K day^{-1} in a small region (SZA=60°) of case 2; and 20 K day^{-1} (SZA=0°) and 10 K day^{-1} (SZA=60°) for case 3. The only $x - z$ cross-section shown is for case 1 with SZA=60° (Figure 8(b)).

Figure 8(c) shows the $x - z$ cross-section of heating rate difference between ICA and 3D in case 1 at $y =$ 36 km for SZA=60°. For individual grid points the differences in heating rate for SZA=0° are in the range between −5 and 5 K day^{-1} for case 1; between −3 and 3 K day^{-1} for case 2; and between −15 and 2 K day^{-1} for case 3. Apart from a small region in case 3, where ICA−3D exceeds −15 K day^{-1}, in general case 1 has the largest 3D effects. It is also found (not shown) that ICA−3D differences are considerably larger in the SZA=60° cases, between −10 and 10 K day^{-1} for cases 1 and 2 and between −15 and 15 K day^{-1} for case 3. This results from a combination of effects. Firstly the larger path length introduces more scattering which exacerbates the 3D effects; secondly the extended illuminated and shadowed regions become relatively more important for lower sun elevations.

For y-averaged $x - z$ sections, the ICA−3D differences are generally less than 0.5 K day^{-1} for SZA=0° in all three cases, with the least in case 1; ICA−3D are less than 1 K day^{-1} for the lower sun and case 1 is the smallest (Figure 8(d)). Similar to the 3D grids, the larger ICA−3D values are seen at SZA=60° than at SZA=0°; in contrast, case 3 has the largest and case 1 the smallest ICA−3D for the y-averaged heating fields.

Figure 9 shows scatterplots of heating rate at SZA=0° and 60° for the three cases. It can be seen that SZA has a very large effect on the ICA−3D difference.

4.2. Short-wave fluxes and radiative properties

Table VI presents the mean albedo, r_t, at the top of clouds for five zenith angles. The definition of r_t is:

$$r_t = F^{\uparrow}(z_t)/F^{\downarrow}(z_t), \tag{3}$$

where z_t represents the height of the cloud top, and $F^{\uparrow}(z_t)$ and $F^{\downarrow}(z_t)$ are mean upwelling and downwelling short-wave fluxes respectively at the cloud top.

It can be seen that the ICA−3D differences for all three cases and five zenith angles are very small (within 1%). However, all the percentage RMS differences exceed 5% and for case 1 the RMS difference exceeds 15% at all SZA. It also can be seen that the percentage RMS difference varies very little for SZAs from 0 to 60° but increases greatly for 80°. This is due to the competing effects of extended illuminating and shadowing, not represented in ICA, versus reduced incoming flux.

Figures 10 and 11 show the 3D albedo at the top of the cloud and the ICA−3D difference in albedo, respectively, for SZA=0° and 60°. Case 1 has the largest local ICA−3D difference and case 2 the smallest. Figure 10

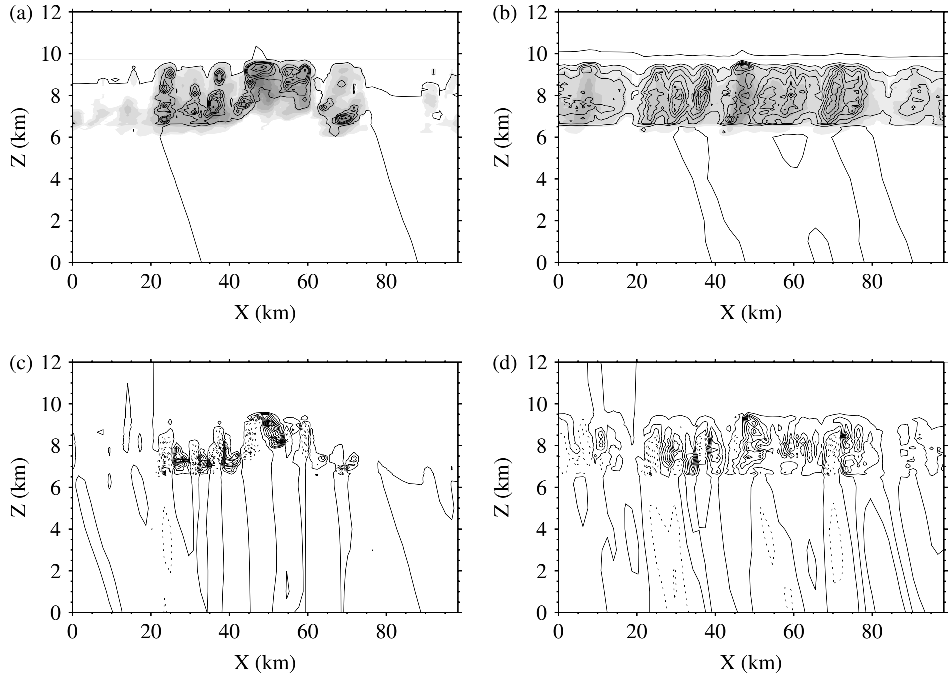

Figure 8. (a) $x - z$ cross-section of short-wave heating rate at $y = 36$ km for case 1, SZA=60°; the contour intervals are 3 K day^{-1} from 1 to 13 K day^{-1} and 12 K day^{-1} from 13 to 40 K day^{-1}. Shading indicates ice water content (light to dark) at 0.001, 0.003, 0.01, 0.03, 0.1, 0.3 g m^{-3}. (b) is as (a) but averaged along the Y direction, with contour interval for heating rate 0.3 K day^{-1}. (c) is as (a) but for difference ICA−3D, with contour interval 1 K day^{-1}. (d) is as (b) but for difference ICA−3D, with contour interval 0.1 K day^{-1}.

Copyright © 2007 Royal Meteorological Society

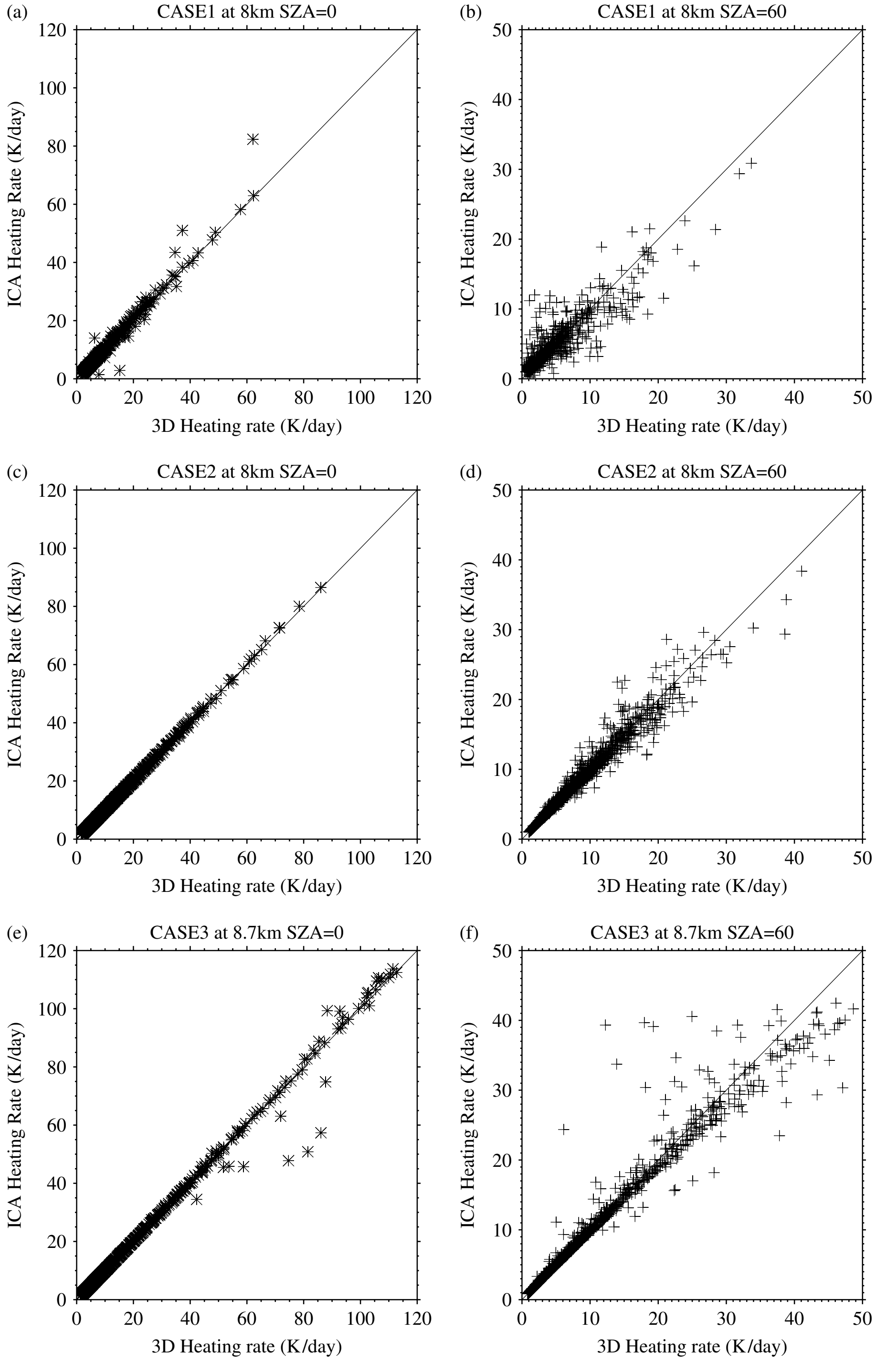

Figure 9. Scatterplots of short-wave heating rate of ICA versus 3D for case 1 and (a) SZA=0° and (b) SZA=60°. (c, d) and (e, f) are as (a, b), but for cases 2 and 3, respectively.

Table VI. Mean albedo at top of cloud, r_t, ICA−3D difference and RMS difference.

	Case 1			Case 2			Case 3		
SZA	r_t	ICA−3D	RMS	r_t	ICA−3D	RMS	r_t	ICA−3D	RMS
0°	0.1841	−0.0010	0.031 (16.8%)	0.2916	−0.0002	0.020 (6.9%)	0.4579	−0.0056	0.030 (6.6%)
20°	0.1871	−0.0003	0.030 (16.2%)	0.3013	0.0016	0.020 (6.7%)	0.4690	−0.0031	0.028 (6.0%)
40°	0.1998	−0.0003	0.031 (15.5%)	0.3341	0.0007	0.019 (5.7%)	0.5076	−0.0012	0.025 (5.0%)
60°	0.2314	−0.0014	0.036 (15.4%)	0.4050	0.0011	0.027 (6.7%)	0.5729	0.0005	0.034 (5.9%)
80°	0.3408	−0.0227	0.105 (30.7%)	0.5555	−0.0023	0.100 (17.9%)	0.6543	0.0009	0.107 (16.4%)

Copyright © 2007 Royal Meteorological Society

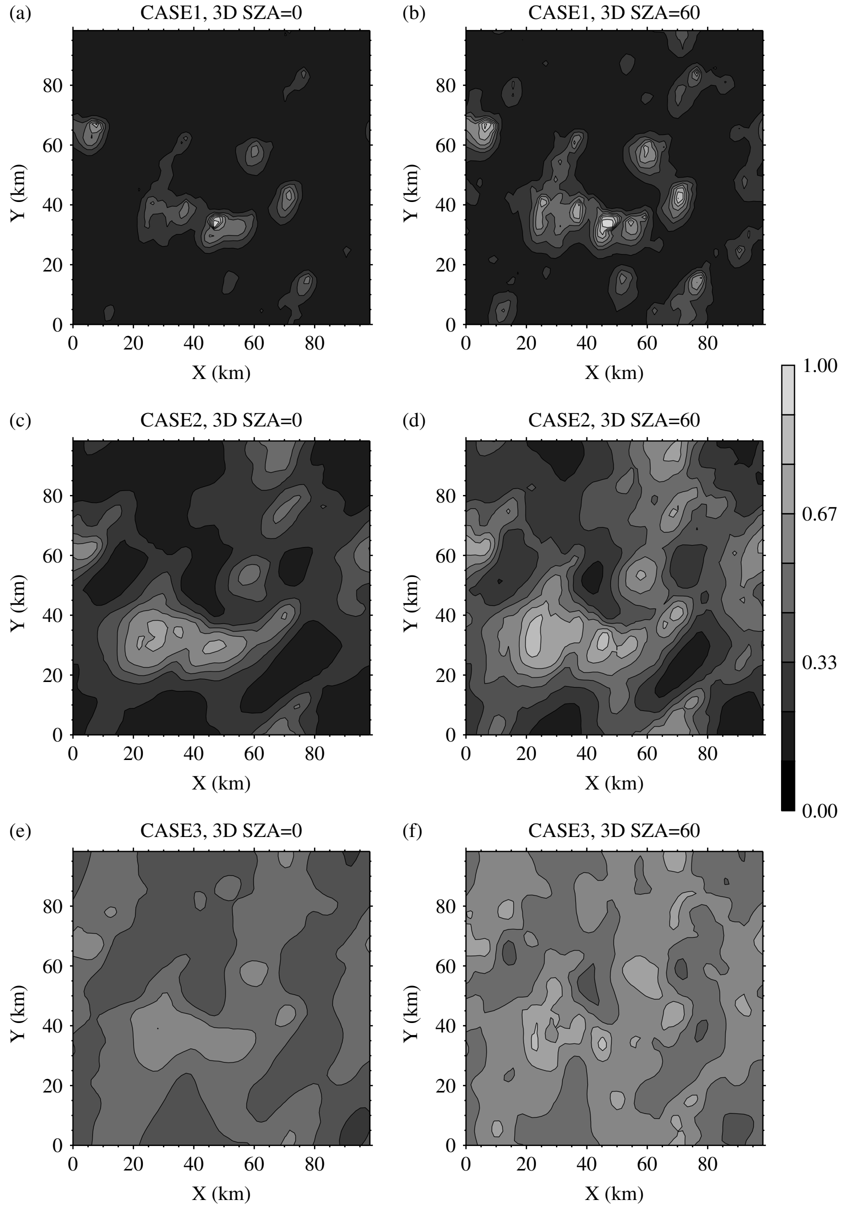

Figure 10. 3D short-wave albedo at top of clouds for case 1 and (a) SZA=0° and (b) SZA=60°. The contour interval is 0.11. (c, d) and (e, f) are as (a, b), but for cases 2 and 3, respectively.

also shows stronger 3D effects on cloud-top albedo for SZA=60° than SZA=0° in all three cases.

We use the following equations to calculate domain-averaged reflectance, transmittance and absorptance:

$$R_{\mathrm{sw}} = F^{\uparrow}(z_{\mathrm{toa}})/F^{\downarrow}(z_{\mathrm{toa}}), \qquad (4)$$

$$t_{\mathrm{sw}} = F^{\downarrow}(z_{\mathrm{surf}})/F^{\downarrow}(z_{\mathrm{toa}}), \qquad (5)$$

$$a_{\mathrm{sw}} = 1 - R_{\mathrm{sw}} - t_{\mathrm{sw}}, \qquad (6)$$

where R_{sw} is the short-wave reflectance at the top of the atmosphere; t_{sw} the short-wave transmittance to the surface and a_{sw} the short-wave absorptance. z_{toa} and z_{surf} are the heights of the top of the atmosphere and the surface, respectively.

R_{sw} and t_{sw} are normalized (divided by $F^{\downarrow}(z_{\mathrm{toa}})$) layer-averaged $F^{\uparrow}$ at the top of the atmosphere and $F^{\downarrow}$ at the surface, respectively. As with the averaged long-wave emissivity, it is found that the differences between averages of $x - y$ 2D reflectance/transmittance/absorptance and those calculated with the averaged relevant fluxes were negligible. We have used those calculated from the corresponding 2D values.

Figure 12 shows the short-wave radiative properties of reflectance, transmittance and absorptance for 3D and ICA calculations as a function of SZA. It is seen that the reflectance is generally enhanced for all SZAs from 3D calculations, although the effect is small especially for case 2. The differences between ICA and 3D in transmittance (Figure 12(b, e, h)) show a similar tendency for the three cases; from negative for higher sun positions, it increases with SZA to near zero for case 3 and even to positive for the other two cases. For all three cases, ICA overestimates the short-wave absorption of the whole

Copyright © 2007 Royal Meteorological Society

DOI: 10.1002/qj

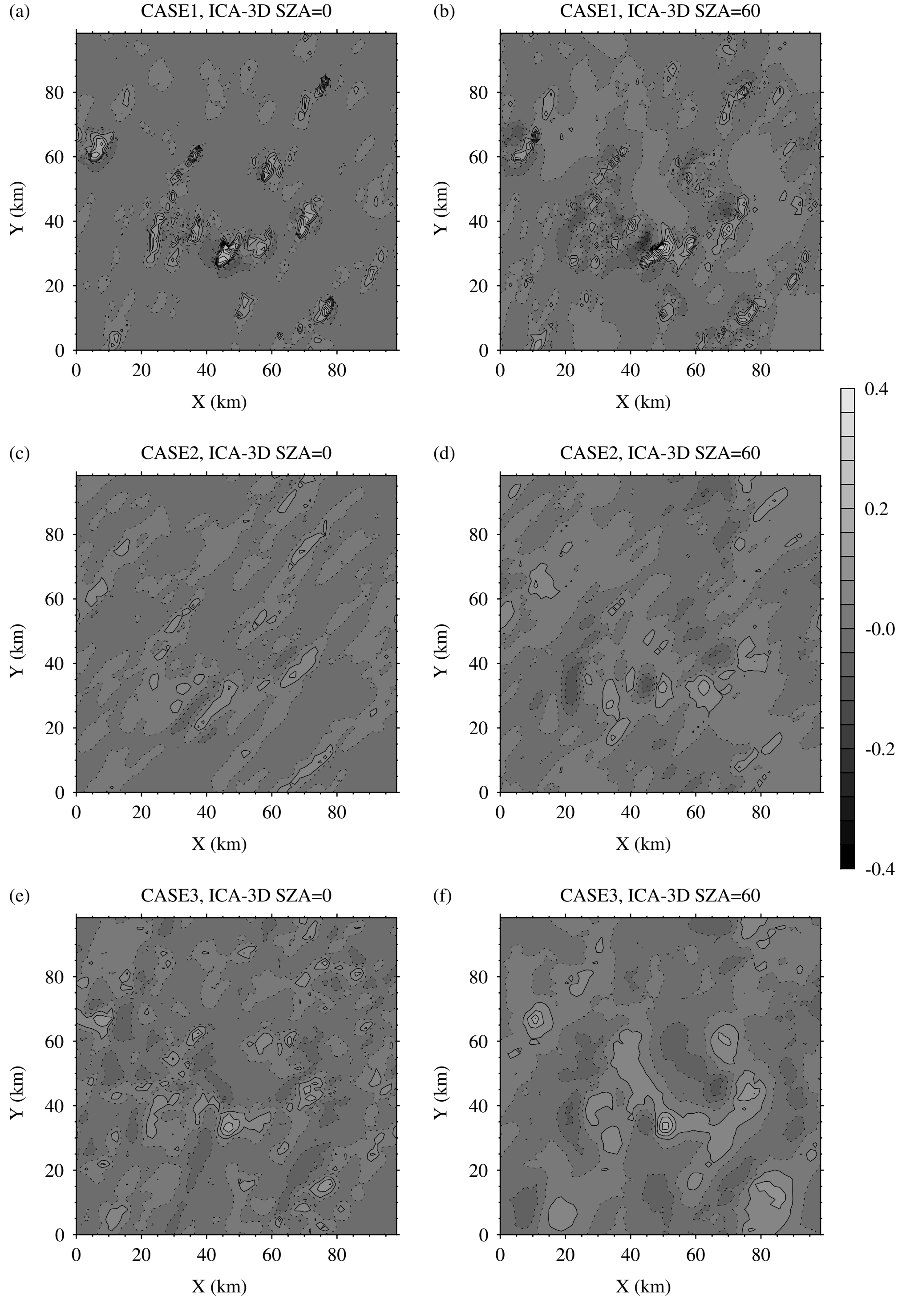

Figure 11. As Figure 10, but for ICA−3D differences in short-wave albedo at top of clouds. The contour interval is 0.04.

domain but the ICA bias decreases with SZA except for case 1 in which ICA−3D difference shows a minimum near SZA=40°. This results from reduced clear-sky absorption because less radiation passes through for the enhanced cloud absorption in 3D radiative transfer.

To a limited extent, the short-wave differences between ICA and 3D in the complex geometry of fall-streak cirrus can be explained in terms of a combination of two effects that occur only in a 3D scenario: escape of photons from the sides of clouds, and shadowing. These effects were used by Gounou and Hogan (2007) to explain differences in the much simpler geometry of an aircraft contrail, but the same mechanisms should apply in more complex scenarios. For example, Figure 12(b) shows that at large solar zenith angles, the ICA reflectance is much lower than 3D in case 1 (the most optically thin case). This can be explained by shadowing, particularly relevant in case 1 which is partially cloudy; at high solar zenith angles,

Copyright © 2007 Royal Meteorological Society

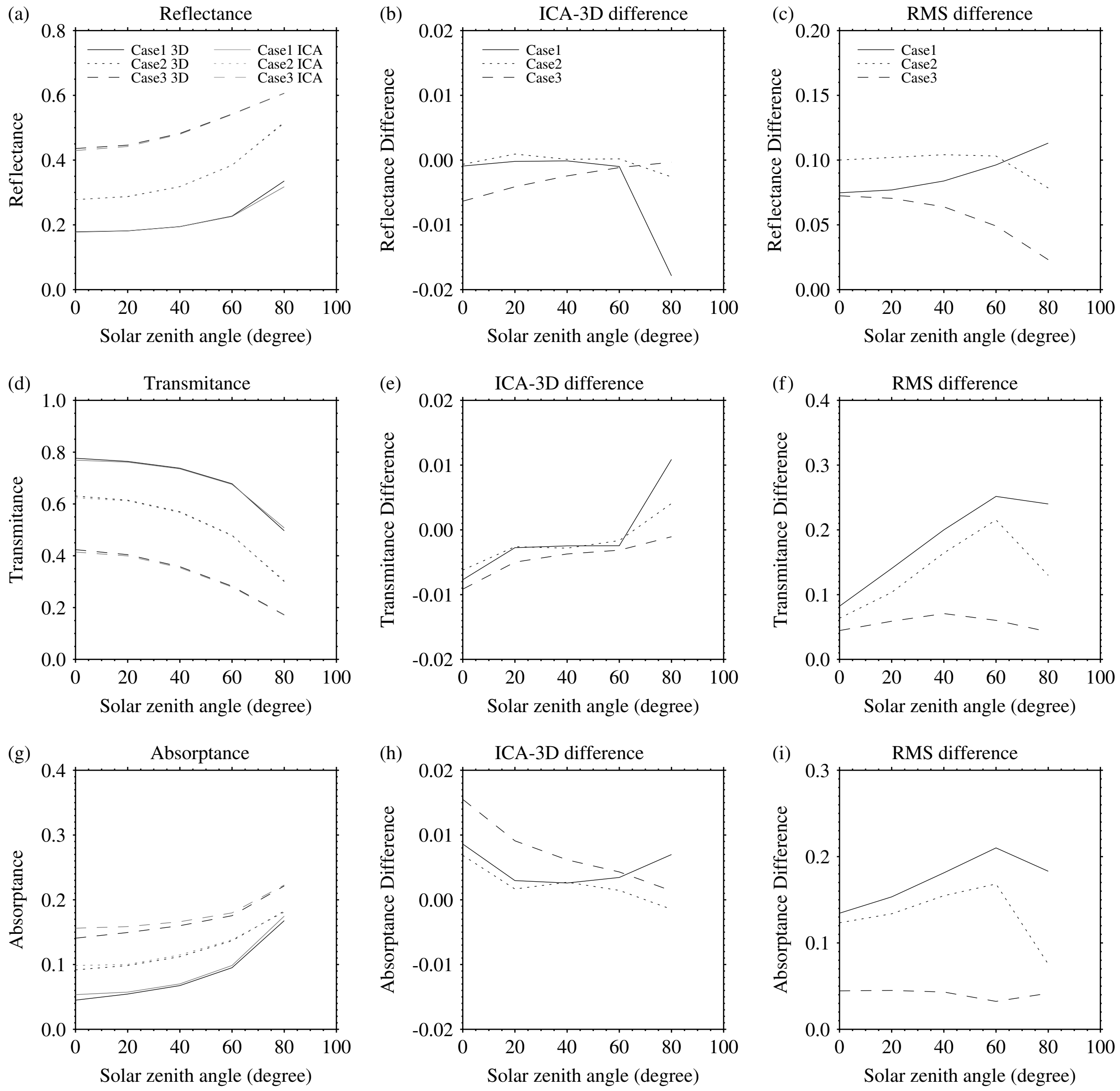

Figure 12. (a) Short-wave reflectance, (b) corresponding ICA−3D differences, and (c) RMS differences, all as a function of SZA for 3D (black line) and ICA (grey line) for the three cases. (d–f) and (g–i) are as (a–c), but for transmittance and absorptance, respectively.

the probability of an incoming solar photon of passing through a cloud is much higher than at low SZAs for the 3D case, but is the same for the ICA case. This leads to a higher reflectance and a lower transmittance for the 3D case at high SZAs. As shown by Figure 7(b), it also leads to greater heating rates.

The RMS differences between ICA and 3D of reflectance, transmittance and absorptance (Figure 12(c, f, i)) are much greater than in Figure 12(b, e, h). For the domain-averaged reflectance and transmittance, ICA agrees with 3D within 5%, similar to the results found by Chýlek and Dobbie (1995). But for domain-averaged absorptance we find that the ICA error can reach 20%, considerably larger than that of Chýlek and Dobbie (1995). Table VII shows the comparison between percentage ICA−3D and percentage RMS differences. The percentage changes of RMS difference show certain trends with SZA. Except for a few individual values, the percentage RMS differences of reflectance and absorptance decrease with SZA, but the percentage RMS difference of transmittance increases with SZA for all cases.

5. Conclusions

In this paper we have analysed the 3D radiative transfer calculations from three realistic representative midlatitude cirrus clouds reconstructed using Hogan and Kew's (2005) stochastic cirrus model, based on the radar data at Chilbolton in southern England. The three cases have different cloud coverages, spatial structures and total optical thicknesses with which we quantify and compare the 3D radiative effects. In this study we focused on the difference between ICA and 3D results, although the plane-parallel 1D results were also discussed.

Unlike water clouds, our long-wave results show that scattering processes are important for cirrus clouds and

Table VII. Percentage ICA−3D difference and RMS difference in domain-averaged short-wave reflectance, transmittance and absorptance.

SZA	Case 1			Case 2			Case 3		
	R_{sw}	ICA−3D (%)	RMS (%)	R_{sw}	ICA−3D (%)	RMS (%)	R_{sw}	ICA−3D (%)	RMS (%)
0°	0.1784	−5	42	0.2778	−0.3	36	0.4358	−1	17
20°	0.1815	−0.1	42	0.2870	0.3	36	0.4461	−1	16
40°	0.1945	−0	43	0.3179	0	33	0.4823	−0.5	13
60°	0.2268	−0.4	42	0.3842	0	27	0.5421	−0.2	9
80°	0.3355	−5	34	0.5168	−0.5	15	0.6066	−0	4
SZA	t_{sw}	ICA−3D (%)	RMS (%)	t_{sw}	ICA−3D (%)	RMS (%)	t_{sw}	ICA−3D (%)	RMS (%)
0°	0.7766	−1	11	0.6305	−1	10	0.4236	−2	10
20°	0.7641	−0.4	18	0.6146	−0.4	17	0.4044	−1	15
40°	0.7379	−0.3	27	0.5700	−0.5	29	0.3578	−1	20
60°	0.6780	−0.4	37	0.4791	−0.3	45	0.2825	−1	21
80°	0.4967	2	48	0.3007	1	43	0.1720	−0.6	25
SZA	a_{sw}	ICA−3D (%)	RMS (%)	a_{sw}	ICA−3D (%)	RMS (%)	a_{sw}	ICA−3D (%)	RMS (%)
0°	0.0450	19	299	0.0917	0.7	135	0.1406	11	32
20°	0.0544	6	282	0.0984	6	136	0.1495	6	30
40°	0.0675	4	268	0.1121	4	138	0.1599	4	27
60°	0.0951	4	221	0.1367	2	123	0.1754	2	18
80°	0.1677	4	109	0.1825	0.6	41	0.2214	0.6	19

they cannot be treated as black bodies in the long-wave region except for near the base of very thick cirrus clouds (e.g. case 3). In general, 3D effects are larger near the top of the clouds than the base. This is probably due to the greater horizontal inhomogeneity at cloud top (Hogan and Illingworth, 2003) and also due to lower densities near cloud top so that more horizontal transport of photons may occur.

While for all three types of cirrus the axis-averaged differences in long-wave heating rate between ICA and 3D are relatively small (less than 1 K day^{-1} for case 1 and 2 and less than 2 K day^{-1} for case 3), the differences for individual pixels are very large (typically several K day^{-1}). The latter depend much less than the former on the total optical depth and the cloud coverage. This indicates that the spatial structure on small scales can produce significant differences when horizontal transport of photons is included.

On average, the long-wave radiative energy redistribution caused by horizontal fluxes results in more heating. Consequently we found ICA cooling biases for all three cases. For the mean heating rates in the upper layers (8–9.5 km), where cooling dominates, the ICA cooling bias peaks at 4% (case 3); in the lower layers (6–7 km) where heating dominates, the ICA cooling bias reaches 7% (case 1). The domain-averaged differences in long-wave heating rate between ICA and 3D are fairly small (less than 0.1 K day^{-1} for case 1 and 2 and less than a few tenths for case 3). However, the RMS differences between ICA and 3D are nearly an order of magnitude larger, indicating that large local errors exist, which almost completely cancel when domain averages are considered.

An analysis of the RMS differences reveals that for all quantities considered, case 1 always has the largest percentage RMS difference and case 2 the smallest, which gives an indication of the processes involved. In general, case 1 (the thinnest cirrus among the three cases) has the largest absolute and RMS percentage differences (ICA−3D) in long-wave heating rate, flux and emissivity. The smaller fractional cloud coverage allows more horizontal transport of photons, and therefore stronger 3D effects take place. This is consistent with previous studies of short-wave 3D transfer in stratocumulus (e.g. Di Giuseppe and Tompkins, 2003a). Another way of explaining this is to consider that, when considering the radiatively important variables of albedo and emissivity, case 1 is clearly the most horizontally inhomogeneous; this is shown by the density of albedo contours at the edges of the cloud elements in Figure 10. Therefore it is not surprising that case 1 shows the greatest 3D effects (in a relative sense).

For short-wave radiation many of our findings and conclusions are similar to those for the long-wave. For example, the axis-averaged heating rates and differences ICA−3D are much smaller comparing to those of individual cells, and for heating rate and many radiative properties, case 1 has the largest 3D effects.

Unlike the long-wave results, the 3D effects in short-wave heating rate are not only important in the cloudy regions but also significant in the clear-sky atmosphere. Another distinct feature is the variation of short-wave 3D effects with SZA. For many radiative quantities, the ICA−3D differences and RMS differences increase when SZA increases. For example, the RMS differences in heating rate approximately double from SZA=0° to

SZA=60°. This is also true for downwelling flux at the surface and domain-averaged transmittance. This implies that the 3D effects may become stronger in extended illuminated and shadowed regions. However, the RMS percentage differences in TOA upwelling flux, domain-averaged reflectance and absorptance all decrease when SZA increases, since for higher sun less radiation is reflected and more photons can be horizontally transported near the top of clouds.

Large local ICA−3D differences are found in heating rate, fluxes and other radiative properties within individual grids. This may have implications for cirrus cloud formation and lifetime; comparison of results from cloud-resolving models with and without radiation showed that radiative heating could enhance cellular structure in cloud layers and increase the cloud lifetime (Dobbie and Jonas, 2001). The large local differences in heating rate between ICA and 3D found in this work would likely influence the dynamics, such as vertical velocity, and thus the inhomogeneity of cirrus cloud, thereby modifying cloud structure and lifetime. More work needs to be done to investigate this effect.

1D calculations produce very large errors compared with domain-averaged 3D in almost all cases. Thus, sub-grid parametrization of cloud inhomogeneity is necessary for the treatment of radiative transfer in cirrus clouds in GCMs.

We analysed only three midlatitude cirrus cases, so the results are indicative for this region. Similar analyses will be of interest for studying the dynamical response to 3D heating in tropical cirrus in which there may be a significant larger-scale impact on cross-tropopause transport.

Acknowledgements

This work was supported by the EC SCOUT-O3 project. We thank Frank Evans for advice on the use of the SHDOM code.

References

Barker HW, Davies JA. 1992. Solar radiative fluxes for broken cloud fields above reflecting surfaces. *J. Atmos. Sci.* **49**: 749–761.

Cahalan RF, Ridgeway W, Wiscombe WJ, Bell TL, Snider JB. 1994. The albedo of fractal stratocumulus clouds. *J. Atmos. Sci.* **51**: 2434–2455.

Chýlek P, Dobbie JS. 1995. Radiative properties of finite inhomogeneous cirrus clouds: Monte Carlo simulations. *J. Atmos. Sci.* **52**: 3512–3522.

Corti T, Luo BP, Peter T, Vomel H, Fu Q. 2005. Mean radiative energy balance and vertical mass fluxes in the equatorial upper troposphere and lower stratosphere. *Geophys. Res. Lett.* **32**(6): L06802.

Dessler AE, Minschwaner K, Weinstock EM, Hintsa EJ, Anderson JG, Russell JM. 1996. The effects of tropical cirrus clouds on the abundance of lower stratospheric ozone. *J. Atmos. Chem.* **23**: 209–220.

Di Giuseppe F, Tompkins AM. 2003a. Three-dimensional radiative transfer in tropical deep convective clouds. *J. Geophys. Res.* **108**: 4741, DOI:10.1029/2003JD003392.

Di Giuseppe F, Tompkins AM. 2003b. Effect of spatial organization on solar radiative transfer in three-dimensional idealized stratocumulus cloud fields. *Atmos. Res.* **60**: 1774–1794.

Dobbie S, Jonas P. 2001. Radiative influences on the structure and lifetime of cirrus clouds. *Q. J. R. Meteorol. Soc.* **127**: 2663–2682.

Evans KF. 1998. The spherical harmonics discrete ordinate method for three-dimensional atmospheric radiative transfer. *J. Atmos. Sci.* **55**: 429–446.

Evans FK, Wiscombe WJ. 2004. An algorithm for generating stochastic cloud fields from radar profile statistics. *Atmos. Res.* **72**: 263–289.

Fu Q, Carlin B, Mace GG. 2000. Cirrus horizontal inhomogeneity and OLR bias. *Geophys. Res. Lett.* **27**: 3341–3344.

Gounou A, Hogan RJ. 2007. A sensitivity study of the effect of horizontal photon transport on the radiative forcing of contrails. *J. Atmos. Sci.* **64**: 1706–1716.

Grabowski WW, Moncrieff MW. 2002. Large-scale organization of tropical convection in two-dimensional explicit numerical simulations. II: Effects of interactive radiation. *Q. J. R. Meteorol. Soc.* **128**: 2349–2376.

Gu Y, Liou KN. 2006. Cirrus cloud horizontal and vertical inhomogeneity effects in a GCM. *Meteorol. Atmos. Phys.* **91**: 223–235.

Haigh JD. 1984. Radiative heating in the lower stratosphere and the distribution of ozone in a two-dimensional model. *Q. J. R. Meteorol. Soc.* **110**: 167–185.

Hignett P, Taylor JP. 1996. The radiative properties of inhomogeneous boundary layer cloud: observations and modelling. *Q. J. R. Meteorol. Soc.* **122**: 1341–1364.

Hogan RJ, Kew SF. 2005. A 3D stochastic cloud model for investigating the radiative properties of inhomogeneous cirrus clouds. *Q. J. R. Meteorol. Soc.* **131**: 2585–2608.

Hogan RJ, Illingworth AJ. 2003. Parameterizing ice cloud inhomogeneity and the overlap of inhomogeneities using cloud radar data. *J. Atmos. Sci.* **60**: 756–767.

Liou KN. 1986. Influence of cirrus clouds on weather and climate processes: a global perspective. *Mon. Weather Rev.* **114**: 1167–1199.

Marshak A, Davis A, Wiscombe W, Cahalan R. 1995. Radiative smoothing in fractal clouds. *J. Geophys. Res.* **100**: 26 247–26 261.

Marsham JH, Dobbie S. 2005. The effects of wind shear on cirrus: A large-eddy model and radar case-study. *Q. J. R. Meteorol. Soc.* **131**: 2937–2955.

McClatchey RA, Fenn RW, Selby JEA, Volz FE, Garing JS. 1972. 'Optical properties of the atmosphere'. Tech. Rep. AFCRL-72-0497, Hanscom Air Force Base: Bedford, Mass., USA.

Mlawer EJ, Taubman SJ, Brown PD, Iacono MJ, Clough SA. 1997. Radiative transfer for inhomogeneous atmosphere: RRTM, a validated correlated-k model for long wave. *J. Geophys. Res.* **102**: 16 663–16 682.

Nikolaeva OV, Bass LP, Germogenova TA, Kokhanovsky AA, Kuznetsov VS, Mayerm B. 2005. The influence of neighbouring clouds on the clear sky reflectance studied with the 3-D transport code RADUGA. *J. Quant. Spectrosc. Radiat. Transfer* **94**: 405–424.

Schlimme I, Macke A, Reichardt J. 2005. The impact of ice crystal shapes, size distributions, and spatial structures of cirrus clouds on solar radiative fluxes. *J. Atmos. Sci.* **62**: 2274–2283.

Tompkins AM, Di Giuseppe F. 2003. Solar radiative biases in deep convective regimes: Possible implications for dynamical feedback. *Q. J. R. Meteorol. Soc.* **129**: 1721–1730.

Várnai T, Marshak A. 2003. A method for analyzing how various parts of clouds influence each other's brightness. *J. Geophys. Res.* **108**: D22 DOI:10.1029/2003JD003561.

Yang P, Liou KN, Wyser K, Mitchell D. 2000. Parameterisation of scattering and absorption properties of individual ice crystals. *J. Geophys. Res.* **105**: 4699–4718.

Copyright © 2007 Royal Meteorological Society